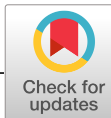

OPTICS

Minimal-gain-printed silicon nanolaser

Byoung Jun Park[1]†, Min-Woo Kim[2]†, Kyong-Tae Park[2], Hwi-Min Kim[1,3], Byeong Uk You[1], Aran Yu[1], Jin Tae Kim[4], You-Shin No[2]*, Myung-Ki Kim[1,5,6]*

Copyright © 2024 The Authors, some rights reserved; exclusive licensee American Association for the Advancement of Science. No claim to original U.S. Government Works. Distributed under a Creative Commons Attribution NonCommercial License 4.0 (CC BY-NC).

While there have been notable advancements in Si-based optical integration, achieving compact and efficient continuous-wave (CW) III-V semiconductor nanolasers on Si at room temperature remains a substantial challenge. This study presents an innovative approach: the on-demand minimal-gain-printed Si nanolaser. By using a carefully designed minimal III-V optical gain structure and a precise on-demand gain-printing technique, we achieve lasing operation with superior spectral stability under pulsed conditions and observe a strong signature of CW operation at room temperature. These achievements are attributed to addressing both fundamental and technological issues, including carrier diffusion, absorption loss, and inefficient thermal dissipation, through minimal-gain printing in the nanolaser. Moreover, our demonstration of the laser-on-waveguide structure emphasizes the integration benefits of this on-demand gain-printed Si nanolaser, highlighting its potential significance in the fields of Si photonics and photonic integrated circuits.

Downloaded from https://www.science.org at Konkuk University Seoul on September 19, 2024

INTRODUCTION

With the use of advanced compound epitaxial techniques capable of fabricating superior optical gain structures, such as multiquantum wells (MQWs), the integration of III-V materials on Si platforms is considered among the most feasible and promising approaches for producing laser-on-Si structures (*1*–*6*). Accordingly, numerous approaches relying on the flip-chip method (*7*, *8*), adhesive wafer bonding via thermosetting polymers (*9*–*12*, *13*), and die-to-die/wafer bonding combined with low-temperature plasma-assisted processes (*12*–*21*) have facilitated successful realizations of III-V microlasers on Si substrates, further demonstrating hybrid and/or evanescent coupling to Si waveguides (WGs). However, in addition to the limitations of the rugged flip-chip process resulting in imprecise/inaccurate alignments and the inefficient use of III-V materials in the heterogeneous/hybrid wafer-bonding technique, the realization of thermally stable, low-power, and noncryogenic continuous-wave (CW) Si-integrable nanolasers with device footprints of a few cubic micrometers remains elusive owing to several fundamental and technical issues: First, most semiconductor nanolasers require large volumes of active media that are typically greater than the resonant lasing modes supported by nanocavities to attain the transparency condition (*22*–*26*). Consequently, with the exception of the mode volume directly associated with lasing, the remaining active medium acts as a massive background absorption agent, resulting in an increased lasing threshold. Second, substantial amounts of excited carriers in high-injection environments diffuse along lateral directions and inevitably result in frustrated carrier confinement (*22*, *25*, *26*). This subsequently causes delocalized radiative and nonradiative recombination. Third, the absorptive part of the active medium and an extended area wherein carrier diffusion occurs still exhibit carrier recombination, contributing to a global increase in the temperature of the entire laser device. This critically hampers the thermal stability and spectral integrity of the laser device under CW pumping conditions. To address these issues, several breakthrough ideas based on optimal minimization of the active media have been demonstrated through enhancing thermal conductivity (*27*), using state-of-the-art selective area regrowth technologies (*28*, *29*), and implementing cavity-localized nano-island gain mapping via time-sensitive digital etching (*30*, *31*). However, despite substantial progress in carrier and optical confinements and the corresponding achievement of low lasing thresholds, access to specialized regrowth technology has been rather limited. Moreover, etching-enabled nanoscale gain mapping is known to induce a thin layer of air gap between the epitaxial structures, rendering the entire cavity structure mechanically fragile. Fourth, from an integration perspective, the nature of the wavelength-scale volumes of lasing modes that are sensitively altered in response to minor structural or environmental variations renders the use of previously adopted integration strategies challenging (*7*–*17*). In particular, coupled with the issues associated with large integration areas and a series of postfabrication steps following III-V integration, critical challenges with regard to insufficient levels of precision and alignments and inaccurate on-demand addressability may result in increased scattering losses and weakening of field confinements. Thus, larger gain volumes than those affordable by current devices are required. Last, the absence of a sufficient heat sink in the vicinity of the nanocavities complicates the realization of thermally stable operations with high spectral integrities under CW conditions. Consequently, all the foregoing combined effects may result in lasing suppression or excessive increase in thresholds, even under the restricted conditions of low-temperature and/or low-duty pulsed excitations. Inevitably, these fundamental and technical issues have motivated researchers to pursue a new breakthrough approach for realizing nanolaser-on-Si structures. However, such an approach must address the unnecessary background absorption, inefficient carrier and optical confinement, and excessive heating issues. Further, it should enable individually addressable, precisely aligned, and on-demand integration without resulting in substantial optical losses, severe operational constraints, and premature performance degradation; moreover, it must circumvent the need to sacrifice a large area of integration and efficient material use.

[1]KU-KIST Graduate School of Converging Science and Technology, Korea University, Seoul 02841, Republic of Korea. [2]Department of Physics, Konkuk University, Seoul 05029, Republic of Korea. [3]Department of Electrical Engineering and Computer Sciences, University of California, Berkeley, CA 94720, USA. [4]Quantum Technology Research Department, Electronics and Telecommunications Research Institute (ETRI), Daejeon 34129, Republic of Korea. [5]Center for Quantum Information, Korea Institute of Science and Technology (KIST), Seoul 02792, Republic of Korea. [6]Department of Integrative Energy Engineering, College of Engineering, Korea University, Seoul 02841, Republic of Korea.
*Corresponding author. Email: ysno@konkuk.ac.kr (Y.-S.N.); rokmk@korea.ac.kr (M.-K.K.)
†These authors contributed equally to this work.

With the above background, this paper proposes an approach for realizing a low-threshold CW integrated Si nanolaser at room temperature (RT) by exploiting a highly precise, aligned, and individually addressable on-demand gain-printing technique. Specifically, the nanolaser uses an optimally designed minimal gain to effectively confine excited carriers and suppress scattering losses while exploiting one-dimensional (1D) absorption-free Si photonic crystals (PhCs) as the primary body of the nanocavity. This facilitates the realization of strong light confinement and high thermal tolerance. The nanolaser can be readily integrated with a conventional strip-type Si WG without requiring complex fabrication steps, thus facilitating its widespread adoption in Si-based photonic systems, and representing an ideal light source for compact Si PICs.

RESULTS AND DISCUSSION

Figure 1A presents a concept schematic of the proposed on-demand gain-printed Si nanolaser. Notably, microstructured polydimethylsiloxane (PDMS)–assisted transfer is known to facilitate highly precise on-demand printing of optically active III-V semiconductor nanostructures on 1D line-defected Si PhCs (*32*, *33*). Following this, the integrated nanoarchitecture results in the formation of a high-quality (high *Q*) optical nanocavity capable of amplifying stimulated light emission, subsequently enabling the realization of strong lasing oscillations. In our study, complete vectorial electromagnetic and charge carrier simulations were adopted to reveal several key features of our device as shown in Fig. 1 (B and C). First, an axially bi-tapered 1D rod-type semiconductor, referred to as a nanoblock (NB), was judiciously designed to minimize optical scattering and not hamper the transmission of light when printed on top of a 1D Si WG (fig. S3). Second, the gradually air-hole-engineered 1D PhCs, coupled with the tapered NB, capitalized on the photonic bandgap (PBG) structures and effectively formed a Gaussian-like photonic well that supported distinct high *Q* optical resonant modes (fig. S4). Consequently, the fields were strongly confined within the gain-printed nanocavity, improving light-matter interactions and resulting in a substantial enhancement in spontaneous emission. Third, the high optical transparency of Si at near-infrared (NIR) frequencies provided an ideal absorption-free mirror to the PBG structure while serving the tapered NB as an optically lossless supporting host (fig. S5). Fourth, a charge transport simulation revealed that III-V/Si heterogeneity fundamentally prohibited the diffusion of minority carriers, which typically reaches an order of a few microns in homogeneous material environments. Moreover, it effectively confines the excited carriers within the volume of the central NB on which the fields of resonant modes are primarily concentrated (Fig. 1C). Notably, such optical transparency and carrier confinement circumvent the critical issues plaguing conventional active III-V semiconductor micro- or nanocavities; these issues include reabsorption of light, reduction in spontaneous emission, delocalized carrier recombination, increased transparent volume of the cavity, and subsequently increased thresholds of lasing operations.

Furthermore, benefitting from the superior thermal conductivity of Si (i.e., $\sigma_{Si} \sim 130$ W/m·K), the PhC host structure exhibits excellent heat drainage within the nanocavity and enables the realization of a steady-state temperature, which is much lower than that of other conventional active semiconductor materials (e.g., GaAs, AlGaAs, InP, and InGaAsP). For direct comparison, we used the 3D finite element method to simulate the heat transfer in our nanocavity structure with Si and InGaAsP host materials (Fig. 1D). Further, visualizations of both the vectorial heat flux and spatial temperature distributions indicated a minor temperature gradient ($\Delta T = T_{max} - T_{min}$) in the Si host structure and a large ΔT in the InGaAsP host structure. Notably, the thermal behavior of the InGaAsP host structure closely paralleled that of a conventional 1D nanobeam PhC structure without a NB (fig. S6). Thus, the numerical study suggested that our device could address issues related to increased heat generation in the nanocavity and facilitate stable operations under high-duty and/or CW conditions.

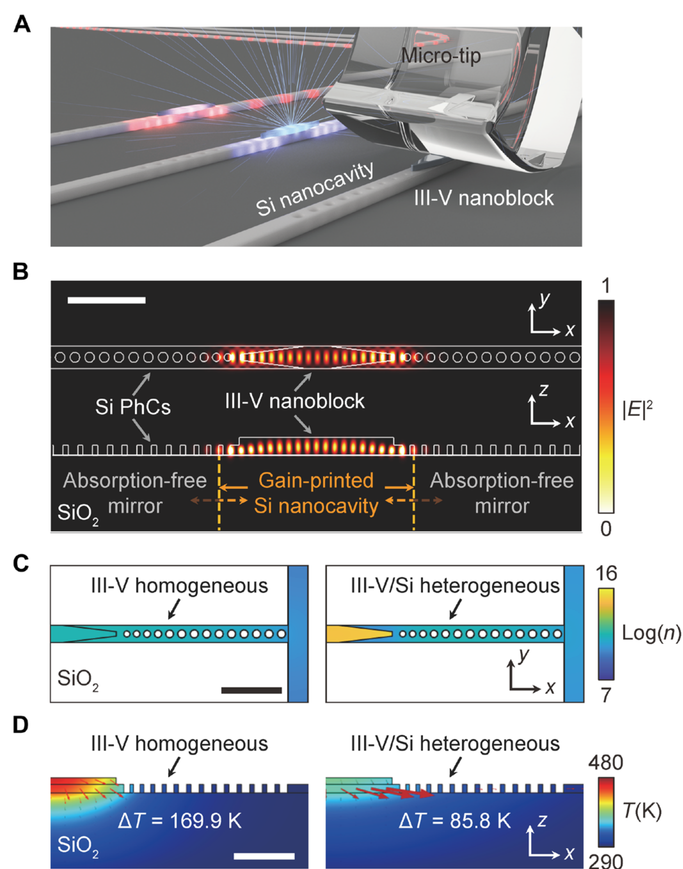

Fig. 1. On-demand minimal-gain-printed Si nanolaser: Numerical characterization. (**A**) Schematic of device exhibiting an on-demand μ-transferred III-V NB on 1D PhC structures defined on a single Si WG. (**B**) Top and side views of the obtained $|E|^2$ profiles of a resonant mode at 1536.8 nm. (**C**) Half-cut top views of a logarithmic plot of the steady-state charge carrier density (*n*) in III-V homogeneous (left) and III-V/Si heterogeneous models (right). (**D**) Half-cut side views of the steady-state temperature distribution (color plots) and vectorial thermal flux (red arrows) in III-V homogeneous (left) and III-V/Si heterogeneous models (right). In the heat transfer simulation, a plane of heat source with 1 mW radiation was introduced at the center of the NB. For all simulations, InGaAsP was considered as the III-V material. All scale bars denote 2 μm.

The device was fabricated based on the following process (Fig. 2). A 220-nm-thick InGaAsP MQW epitaxial slab structure was used to fabricate an array of tapered NBs by using conventional semiconductor microfabrication techniques (presented in Materials and Methods). Scanning electron microscopy (SEM) images presented the structural features of the device (Fig. 2A). A single NB with a length of 4.6 μm was linearly tapered at both ends and tethered to a

Downloaded from https://www.science.org at Konkuk University Seoul on September 19, 2024

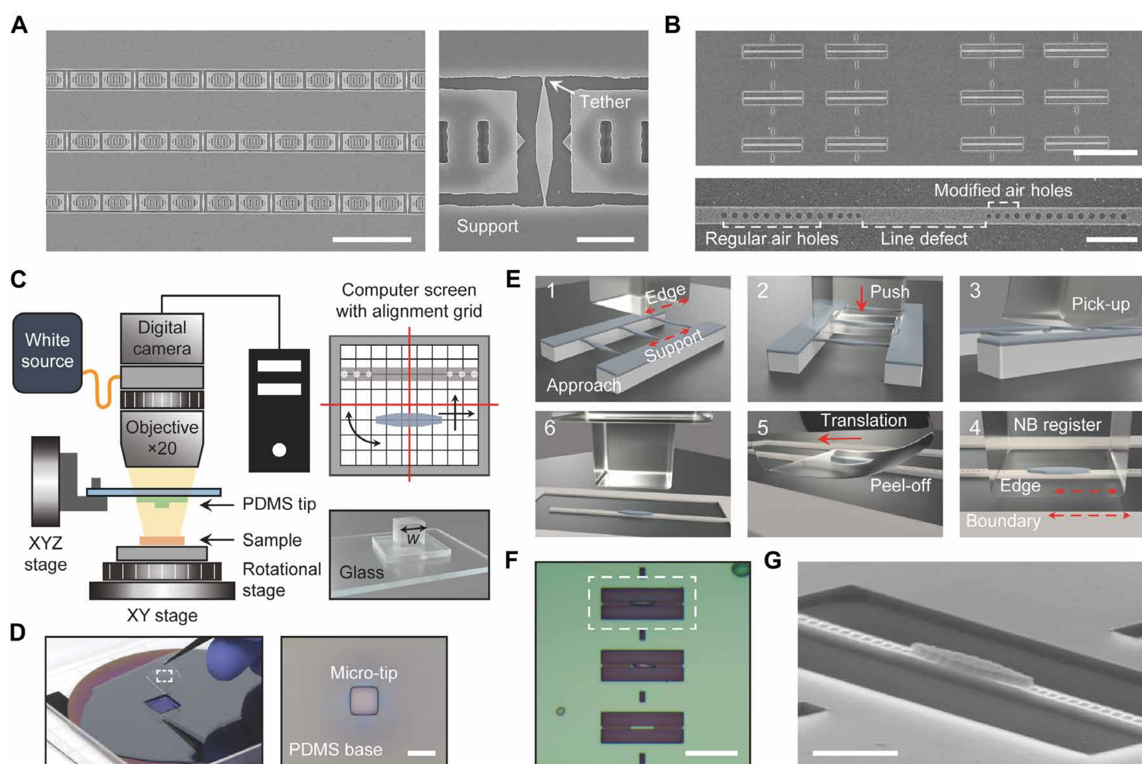

Fig. 2. Device fabrication using the μ-transfer-enabled gain-printing technique. (**A**) SEM images of the free-standing InGaAsP NB array (left) and single NB (right). (**B**) SEM images of the 1D Si PhC array (top) and single Si PhCs (bottom). Scale bars for the array and single devices denote 20 and 2 μm, respectively. (**C**) Schematic of the μ-transfer-printing setup. A cubical PDMS μ-tip with one side of *w* was used in the conventional transfer-print setup. High-precision XYZ stages with nanoscale step sizes were used. (**D**) Image of the fabricated PDMS μ-tip (left). Optical image of a single μ-tip (right). Scale bar denotes 20 μm. (**E**) On-demand addressable gain printing: (1) aligning, (2) breaking terminals, (3) pick-up, (4) align-registration, (5) peeling-off, and (6) pulling-out. (**F**) Optical image of completely fabricated on-demand minimal-gain-printed nanolasers. Scale bar denotes 10 μm. (**G**) Tilted SEM image of the white dotted box in (F). Scale bar represents 2 μm.

supporting bulk slab. In parallel, an array of 1D line-defected PhCs with a width of 660 nm was separately fabricated on a 280-nm-thick Si-on-insulator (SOI) wafer (Fig. 2B). Further, a 5.6-μm-long missing air-hole host region, surrounded by a series of modified and regular air holes, was designed to provide strong support to the fabricated NB. A half-wavelength thin NB (i.e., $t_{NB} \sim \lambda/2n_{NB}$) and a 9° angled bi-taper, coupled with certain graded air-hole modifications, were designed to substantially increase the field overlap between the NB and Si PhCs. Our manufacturing process exhibited an approximate error margin of ±5%, causing a deviation of about ±3 nm from the desired wavelength. Strategically, we fabricated multiple samples with lattice constants varying by ±15 nm. This variation allowed each mode to cover a wide wavelength range of up to ±50 nm.

For the precise, on-demand integration of individual NBs with the 1D PhCs, a previously developed state-of-the-art microtransfer (μ-transfer) technique was used in Fig. 2C (*32*, *34*, *35*). In particular, we fabricated a microcubical structure that protruded out of the base PDMS stamp to enable the realization of target-transfer single microstructures (Fig. 2D). Relevant details on the setup and fabrication of the PDMS microtip (μ-tip) are presented in fig. S7. Typically, on-demand μ-transfer printing involves several key steps, which are schematically described in Fig. 2E: (i) aligning and approaching, (ii) breaking tethers, (iii) picking up and separating, (iv) center-to-center align registering, (v) peeling off, and (vi) pulling out. The optical and SEM images displayed in Fig. 2 (F and G) present the successfully gain-printed Si nanolaser devices and reveal the highly precise integration of the NB with nanoscale alignment accuracy. Notably, a systematic misalignment study (fig. S8) and the results of certain previous studies undoubtedly guaranteed that the proposed μ-transfer printing was highly reliable and reproducible and, thus, readily applicable to various on-demand integration applications requiring both high precisions and alignment accuracies. In addition, the bonding quality of the integration was characterized via high-resolution transmission electron microscopy (fig. S9). The cross-sectional image presented a clean and uniform interface without any irregular voids or air gaps, thus ensuring lossless interaction with light and smooth heat transfer.

Systematic μ-photoluminescence spectroscopy was used to characterize the important optical properties (Figs. 3 to 5 and fig. S10). Note that we used different samples that demonstrated their optimal performance under specific conditions, resulting in variations in the laser wavelength positions. First, light emission with increasing incident peak pump power (P_{peak}) was briefly examined under pulsed pumping conditions. The captured NIR InGaAs camera images displayed in Fig. 3A unambiguously demonstrated three different phases of light emission: spontaneous (SE at below-threshold levels, second panel), amplified spontaneous (ASE at near-threshold levels, third panel), and amplified stimulated (lasing at above-threshold levels, fourth panel) emissions. In particular, the strong and dipole-polarized light emission spots appearing near the

Downloaded from https://www.science.org at Konkuk University Seoul on September 19, 2024

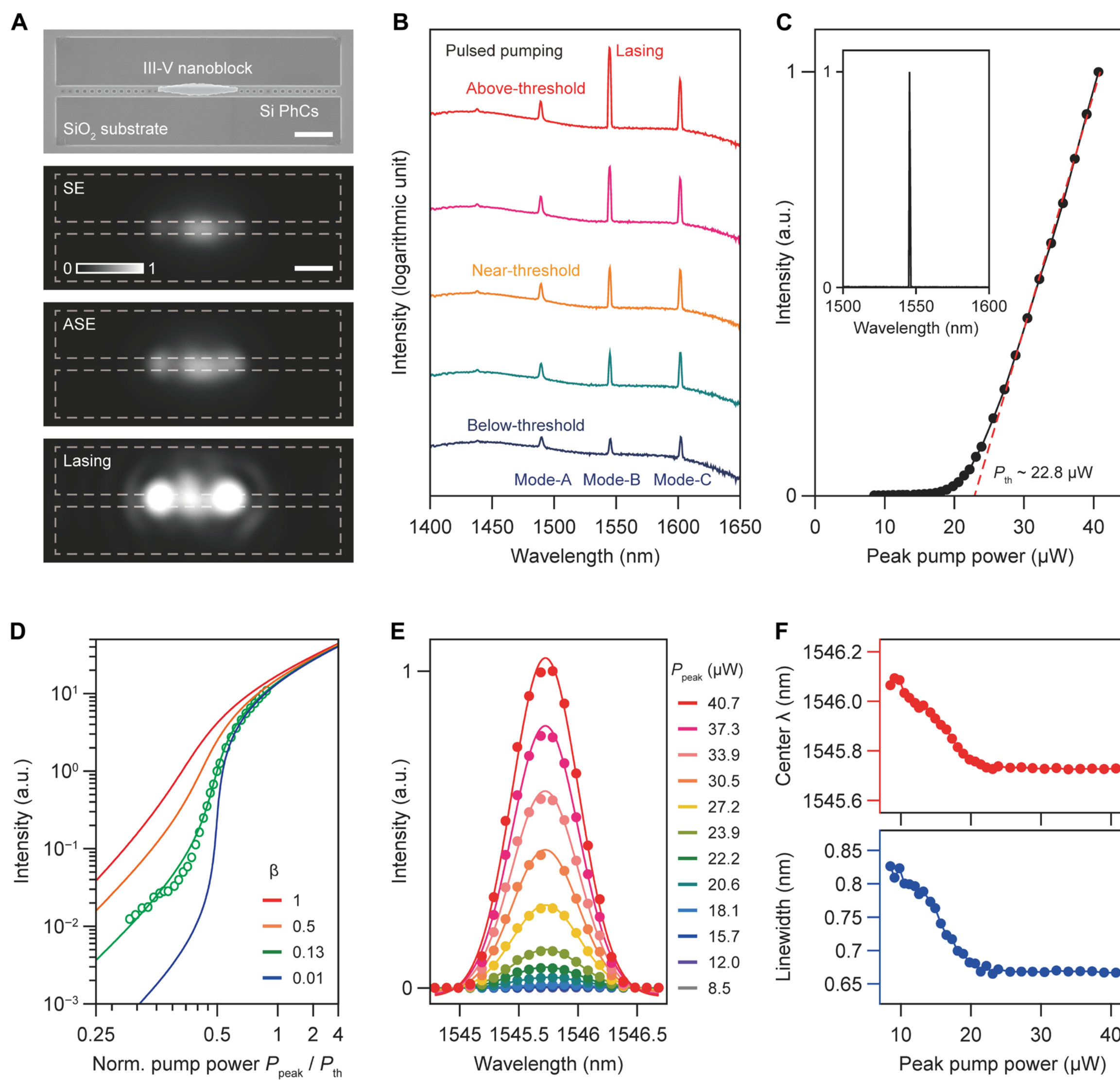

Fig. 3. Pulsed lasing characteristics. (**A**) SEM image of the single laser device and NIR camera images presenting SE, ASE, and lasing actions with increasing P_{peak}. The repetition rate and pulse width of a 976-nm pump laser were 1 MHz and 100 ns, respectively. Scale bars denote 2 μm. (**B**) Recorded spectra at below-, near-, and above-threshold levels revealing modal competition (Mode-A, Mode-B, and Mode-C) and the selection of the lasing mode (Mode-B). (**C**) Laser characteristic curve with P_{th} ~ 22.8 μW. Inset: Recorded lasing spectrum at near P_{th}. (**D**) Rate-equation analysis. *L-L* curve fittings for β = 1 (red), 0.5 (yellow), 0.13 (green), and 0.01 (blue). Experimental data (green-colored open circles) were best fitted with β = 0.13. (**E**) Recorded spectra (dots) and Lorentzian fits (lines) from far-below- (P_{peak} = 8.5 μW) to far-above-threshold (P_{peak} = 40.7 μW) levels. (**F**) Plots of the center wavelength (top) and linewidth (bottom) as a function of P_{peak}.

boundaries of the PhCs and the outwardly spreading interference patterns implied successful lasing oscillations in the device. Further, spectroscopic analyses revealed the competition between resonant modes with increased P_{peak} and lasing mode evolution (Fig. 3B). Below the threshold, three resonant modes were initially excited around the shoulder of the gain PL at 1489.7 (Mode-A), 1545.7 (Mode-B), and 1602.2 (Mode-C) nm. These resonant modes were predicted by numerical simulations (fig. S4) to have high *Q*-factors (>3000), small mode volumes [~2.0 $(\lambda/n)^3$], and to exhibit the same orientational polarization preference. With an increase in P_{peak}, Mode-B grew rapidly in intensity and favorably developed into the lasing mode.

Further, mode-selective optimized pumping facilitated quantitative characterization of the laser (Fig. 3C). The light-in versus light-out (*L-L*) curve exhibited a superlinear increase in intensity with a low-threshold peak pump power (P_{th}) of ~22.8 μW. Further, the rate-equation analysis adopted to best fit the experimental data yielded an estimated spontaneous emission factor (β) of ~0.13 and an internal quantum efficiency (η_i) of ~0.20 for a gain coefficient g_0 of ~3000 cm^{-1} and a *Q*-factor of 5.7×10^3 (Fig. 3D). In addition, the analysis estimated a P_{th} value of ~23.06 μW, which was consistent with the experimental value (Supplementary Note). The laser's output power, collected through an objective lens with a numerical aperture of 0.42, was measured to be approximately 5 nW for P_{peak} of 40 μW.

Spectral development of the lasing mode, further confirming the quality of the device, is shown in Fig. 3 (E and F). Notably, superior

Downloaded from https://www.science.org at Konkuk University Seoul on September 19, 2024

to other active micro- or nanocavity lasers, the proposed device exhibited minimal blue or red shifts of the laser peak from near to far above the threshold (Fig. 3F, top). Moreover, following an abrupt reduction at the near-threshold level consistent with the Schawlow-Townes (ST) behavior (*36*), the laser linewidth robustly remained clamped to a resolution-limited value of ~0.67 nm without further broadening (Fig. 3F, bottom). Consequently, the laser peak exhibited almost identical spectral features over the entire range of lasing operations. Thus, the spectral purity and stability, coupled with the low-threshold value, experimentally validated the results of previous numerical studies. For example, prohibited reabsorption and carrier diffusion/recombination reduced unwanted optical losses and contributed to the realization of a low threshold. In addition, the excellent thermal tolerance of Si firmly stabilized the spectral gain profile and effective refractive index, thus minimizing frequency pulling [$\lambda_{pull} = Q_g/Q_m\ (\lambda_{gmax} - \lambda_m)$] and resonance shifting of the optical modes ($m\lambda_m = 2n_{eff}L_c$). Here, note that λ_{gmax} and λ_m denote the maximum gain wavelength of a material and the resonant mode wavelength with modal index m of a given cavity, respectively; Q_g and Q_m denote the Q-factors of the gain profile and resonant mode, respectively; and n_{eff} and L_c represent the effective refractive index and cavity length, respectively.

Motivated by the results and analysis presented in Fig. 3, we further attempted to demonstrate high-duty and CW operation at RT (Fig. 4 and figs. S11 and S12). Figure 4A illustrates representative emission spectra obtained from one of the best-performing samples under duty cycles of 10 and 50% and CW pumping conditions. The observed sharp lasing peak at 1548.2 nm exhibited spectrally identical features under pulsed conditions, whereas it was slightly red-shifted ($\Delta\lambda_{shift}$ ~ 1.2 nm) and broadened ($\Delta\lambda_{1/2}$ ~ 0.86 nm) under CW incidence. With an increase in the pump power (P_{cw}), typical ST behavior appeared with a rapid linewidth narrowing at $P_{cw} > 50$ μW, indicating initiation of the domination of amplified stimulated emission (StE; Fig. 4B). However, we observed an early rollover of light emission for $P_{cw} > 100$ μW, which indicated performance degradation. These observations can be primarily attributed to increased

Downloaded from https://www.science.org at Konkuk University Seoul on September 19, 2024

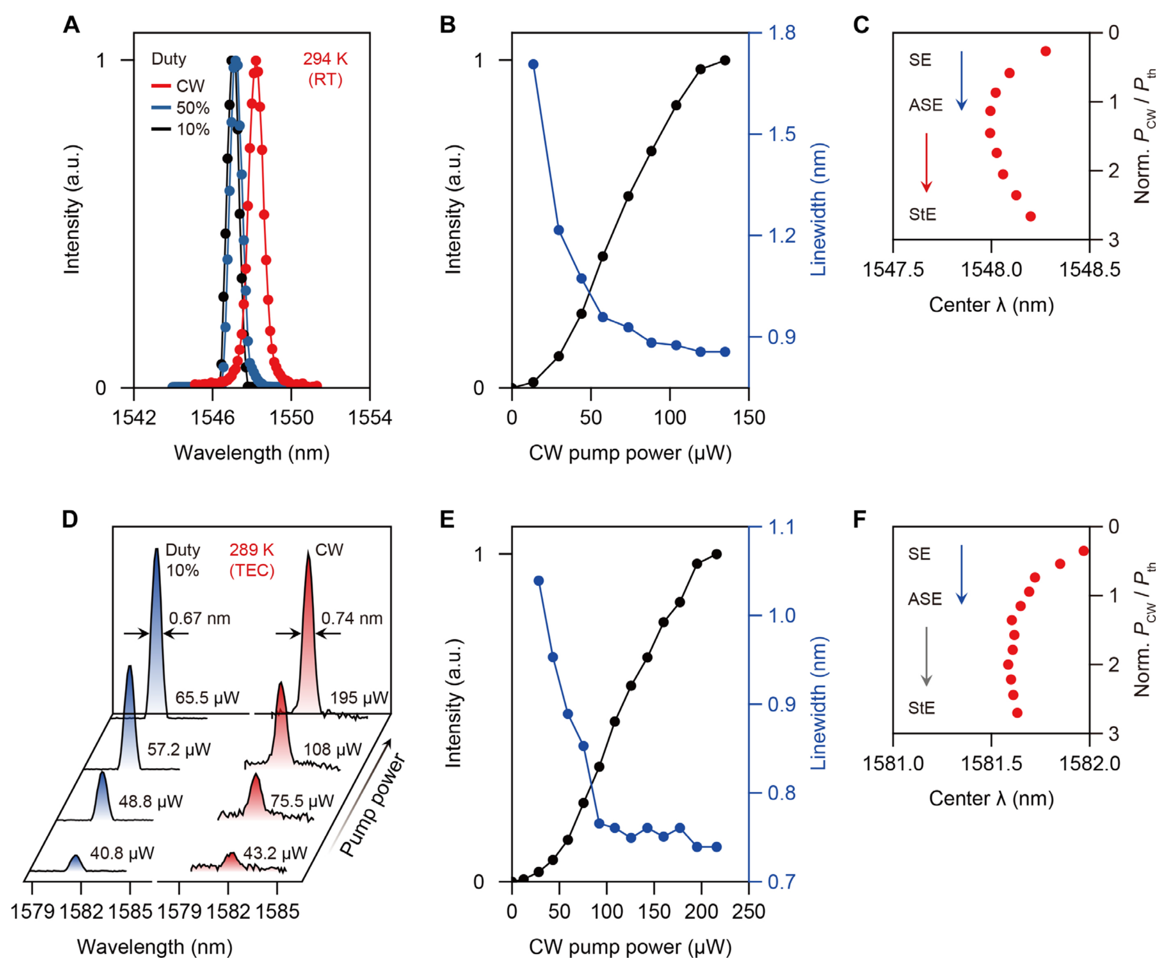

Fig. 4. Emission characteristics under CW pumping. (**A**) Normalized above-threshold lasing spectra at 10% (black) and 50% (blue) duty cycles and under CW (red) conditions at RT. Here, P_{peak} values for 10 and 50% conditions were 93 and 128 μW, respectively, and P_{cw} was 133 μW. The relative ratios of the peak intensity for black, blue, and red are 1.0, 2.5, and 0.6, respectively. (**B**) Emission characteristic curve (black) and linewidth plot (blue) under CW conditions. (**C**) Plots of the peak wavelength as a function of the normalized power P_{cw}/P_{th}, where P_{th} ~ 50 μW. Blue and red arrows represent types of peak shifts occurring while the phase transitions from SE to ASE and stimulated emission (StE). (**D**) Emission spectra of the TEC-cooled device under pulsed (blue) and CW (red) conditions. The chip was noncryogenic and Peltier-cooled at 289 K. For both conditions, P_{peak} and P_{cw} can be visualized inside the panel. (**E**) Emission characteristic curve (black) and linewidth plot (blue) for the TEC-cooled device. (**F**) Plots of the peak wavelength as a function of P_{cw}/P_{th}. The gray arrow represents a suppressed peak shift from ASE to StE transition.

thermal carrier fluctuations and charge carrier scattering in the active region of the NB and a decreased differential quantum efficiency (*37*). Moreover, these combined effects were also observed in the spectral peaks, exhibiting a blue and red shift with a phase transition from SE to ASE and StE in Fig. 4C (*38*–*40*). Further, the heat-draining power of the Si PhCs was inevitably limited to the absolute volume and the fundamental constant of Si; therefore, a fine interplay between pumping conditions and thermal tolerance is essential to achieve the best lasing performance. However, this issue can be addressed with a decrease in the chip temperature by a minor degree in noncryogenic environments as shown in Fig. 4 (D and F). Figure 4D and fig. S13 present several spectra recorded by a laser device that was thermoelectrically cooled by only 5 K (i.e., $T = 289$ K) and operated under both 10% pulsed and CW conditions. As is evident, a strong signature of lasing operation was observed up to a high P_{cw} value of ~200 μW with a much narrower peak linewidth of ~0.74 nm. The characteristic curve and linewidth plot displayed in Fig. 4E exhibited more distinct features than those in Fig. 4B. In addition, spectral purity and stability were restored, exhibiting approximately negligible changes with phase transitions at increasing P_{cw} (Fig. 4F).

Overall, the practical merits of the on-demand integrability of gain and 1D nature of the nanocavity were completely demonstrated in the WG-coupled laser application (Fig. 5). In this device, a simple extension of the Si WG body at one end of the original nanocavity structure facilitated efficient light coupling (Fig. 5A, top). In addition, the rational design of air holes controlled the ratio of the power transmitted toward the WG (P_{trans}) to the total power emitted by the nanolaser (P_{tot}) (Fig. 5A, bottom). Considering the numerical simulation results presented in Fig. 5B, we introduced six air holes to simultaneously achieve a high Q-factor of $>10^4$ for the nanocavity to support lasing oscillations and sufficient light transmission corresponding to $P_{trans}/P_{tot} > 27.1\%$. Evidently, this transmission-controlled nanolaser, in contrast to conventional microlaser-WG integrations requiring a large device footprint and further additions of complexities and delicacies in fabrication, could be designed, and lithographically incorporated by using most conventional Si WGs.

Downloaded from https://www.science.org at Konkuk University Seoul on September 19, 2024

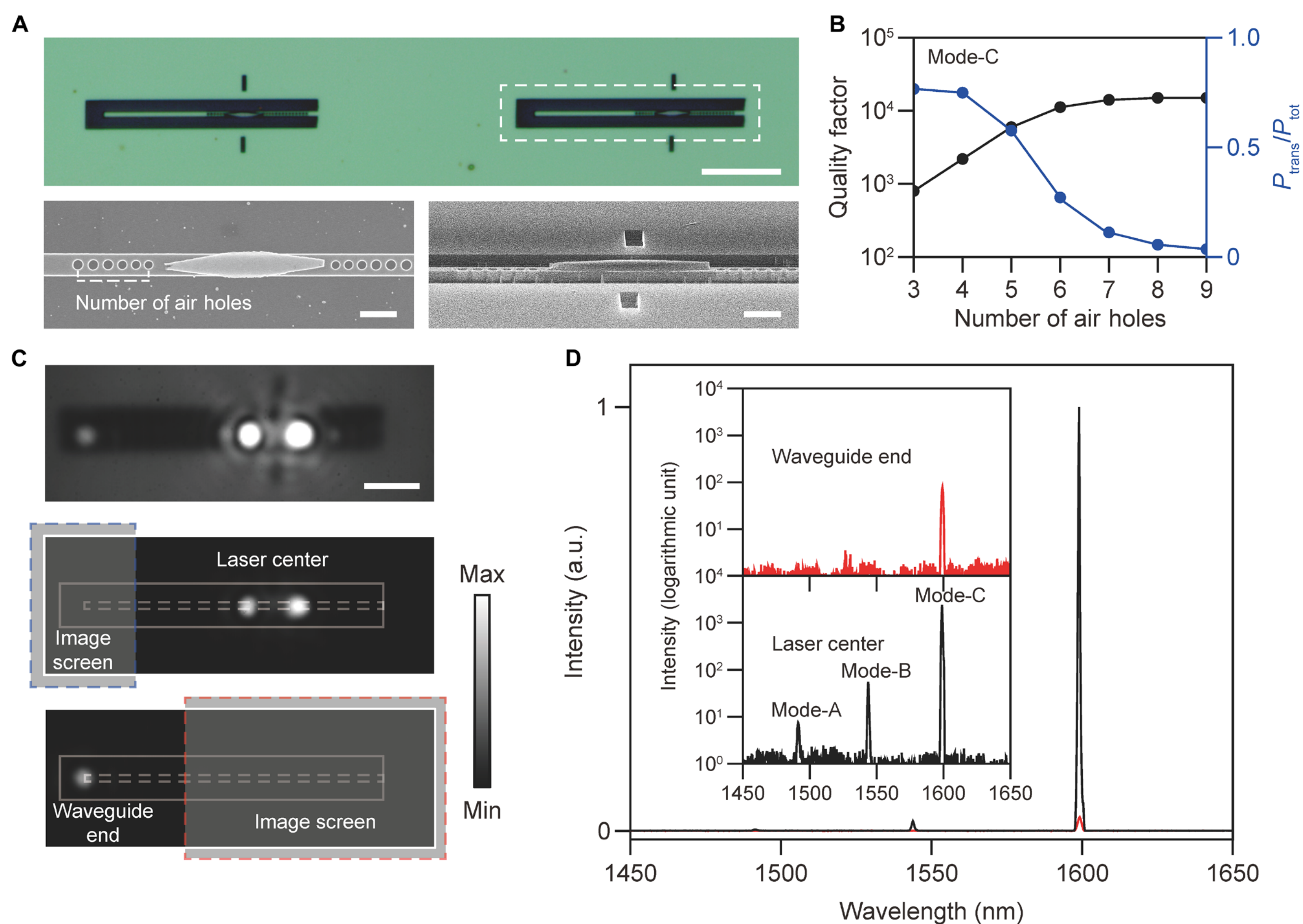

Fig. 5. Laser-on-WG application. (**A**) Optical and SEM images of the on-demand WG-coupled laser device. Scale bar denotes 20 μm. Top and side views of the magnified SEM images depict the device in a white dotted box in the top panel and highlight structural details including modified air holes (left) and the seamless integration of NB with Si PhCs (right). Scale bars denote 1 μm. (**B**) Co plots of the calculated Q-factor (black) and transmission efficiency (P_{trans}/P_{tot}, blue) as a function of the number of air holes. Here, Mode-C is considered as the lasing mode. (**C**) Laser-to-WG coupling experimental results. NIR camera images captured the complete device (top) and either the WG end (blue dotted box, center) or the laser (red dotted box, bottom) screened devices. Scale bar denotes 5 μm. (**D**) Spectra recorded at the center of the laser (black) (middle panel in C) and at the end of the WG (red) (bottom panel in C). Inset: Spectra in logarithmic scale.

In spectroscopic measurements, strongly dipole-polarized laser emission at the center of the WG-coupled device and a bright light spot at the end of the Si WG under pulsed pumping with a duty cycle of 10% were observed as shown in Fig. 5 (C and D). The laser successfully operated at up to a 50% duty cycle (fig. S14) but failed under CW conditions. This limitation is attributed to a reduction in the Q-factor caused by WG coupling, which in turn increases the lasing threshold, approximately six times higher than that in the structure without the WG, accompanied by a consequential rise in heat. This issue could be addressed with more advanced structural design and improved thermal management. In Fig. 5 (C and D), partially screened site-selective measurements revealed several interesting features. First, the nanolaser, as anticipated, supported three resonant modes, indicated as Mode-A, Mode-B, and Mode-C (Fig. 5D, inset). Specifically, the WG-coupled structure exhibited Mode-C at 1599.0 nm as the predominant active lasing mode. This indicated that the structural modifications in the WG-coupled nanolaser additionally introduced unlevelled effects on the mode competition and favorably served Mode-C. The reduction in the number of regular air holes on the WG side enabled partial transmission of light and substantially reduced the reflectivity of the PBG along the direction of the Si WG alongside a decrease in the Q-factor (fig. S15). However, Mode-C, with the highest Q-factor, is more adept at offsetting the decrease in Q-factor due to coupling losses, thereby more efficiently satisfying the criteria for effective laser operation. In addition, considering the transverse-electric-like nature of the PBG, Mode-A and Mode-B, which were more strongly polarized along the TE direction, that is, perpendicular to the PhCs (figs. S16 and S17), experienced more severe optical losses than Mode-C. Second, the spectrum obtained from the WG end exhibited only a single pronounced peak, which corresponded to the lasing mode (Mode-C). This selection, which once again originates from the high Q-factor, including WG coupling loss and the polarization preference, revealed that despite the weakening, the PBG mirror comprising six air holes still served as an efficient stop for Mode-A and Mode-B, whereas Mode-C. Last, the polarization-resolved spectroscopy results support the above findings and analysis by exhibiting a substantial suppression of Mode-A and Mode-B under horizontal polarization (fig. S18).

In summary, a newly developed gain-printed Si nanolaser was proven to be an ideal Si-integrable nanolaser as it addressed several critical issues: on-demand integration with high precision and nanoscale alignment, scattering suppression, frustrated carrier diffusion, reduction of reabsorption, transparent nanocavity, superior thermal stability, and high spectral integrity. In addition, this technology simplifies the manufacturing process compared to epitaxially grown gain structures on Si substrates (*41*–*42*), thereby reducing potential defect densities and allowing for selective adjustment of the spacing and positioning between Si photonics and the gain medium, enhancing design flexibility. Nonetheless, under CW pumping conditions, a reduction in coherence and power stability was still observed in comparison to pulse-pumped scenarios (Supplementary Note). We believe that future advancements in device design and improved thermal management strategies will address these issues (*28*, *43*). Furthermore, combined with the pioneering and advanced carrier injection technologies (*34*), the μ-transfer-printing technique can facilitate an efficient electrification of various on-demand transfer-integrated optical devices for practical applications. This innovative nanolaser can be applied to a conventional Si WG via simple lithographic steps, exhibiting potential for widespread adoption in various Si-based photonic platforms. Moreover, the state-of-the-art μ-transfer-printing technique can be extensively adopted in photonic integration, as well as micro- and/or nano-electronic integration systems.

MATERIALS AND METHODS

Numerical simulations

We obtained the electric field profiles, Q-factors, confinement factors, mode volumes, and resonance wavelengths for the proposed on-demand gain-printed Si nanolaser using the finite-difference time-domain (Lumerical, FDTD Solutions) method. Correspondingly, 3D FDTD simulations were performed with the application of a mesh accuracy of five to automatic nonuniform grids surrounded by a perfectly matched layer (grid resolution was applied below 20 nm near the Si PhCs). The refractive indices of Si, InGaAsP, and SiO_2 were set to 3.45, 3.4, and 1.45, respectively. Perfectly matched layers were applied to the boundary of the simulation region. To obtain the value of the optimal NB parameter, a parameter exhibiting minimal scattering loss when printed on an Si WG was designed. The TE fundamental mode was applied to the Si WGs and after passing through the NB printing region. Further, the transmittance calculation was optimized to minimize scattering losses (fig. S3). The volume of the resonance modes was calculated as the ratio of the total energy density per unit volume to its peak energy density. The optical energy confinement factor was calculated using the ratio of the energy in the InGaAsP QW with a thickness of 220 nm to the total energy. Moreover, the WG coupling efficiency was calculated by determining the ratio of the energy exiting the WG port (P_{trans}) following resonance mode stabilization to the total energy exiting the device (P_{total}). The polarization characteristics were computed by filtering through Jones metrics in the Pz field profile passing 1 μm above the device surface (fig. S16).

For charge simulations, we used the finite element drift-diffusion method (Lumerical, Charge Transport Solver) to calculate the steady-state carrier density. The electron and hole mobilities of InGaAsP were set to 2735.51 and 269.16 cm^2/s, respectively. For other materials (e.g., Si and SiO_2), built-in material parameters were used. To reflect the experimental situation and appropriately introduce a charge source, first, carrier generation with light absorption was analyzed. A 976-nm Gaussian incidence with a spot size of 2 μm that vertically illuminated the center of both the heterogeneous and homogenous models was used. All the boundaries of the simulation domain were grounded ($V = 0$).

For the heat transfer simulation, we used the finite-element method (COMSOL-Multiphysics) to obtain the spatial distribution of temperature and the vectorial heat flux of the device under steady-state conditions. The thermal conductivities of the Si, InGaAsP, and SiO_2 insulator layers were set to 130, 8.50, and 1.40 W/m·K, respectively. A uniform heat source with a radiative power of 1 mW was applied to the thin layer at the center of the NB. Further, the errors attributed to closeness between the fixed temperature boundary and the device were reduced via the application of an infinite element domain at the boundaries, and here, the initial temperature was set to RT (293.15 K). Thermal insulation was applied between the device and air while assuming no air convection.

Fabrication

The NB array was fabricated on an InGaAsP wafer, with a 200-nm-thick InP layer (capping layer), 240-nm InGaAsP layer including seven MQW structures, 400-nm-thick InP layer (sacrificial layer), and an InP substrate. Following brief wet etching of the InP capping layer using a diluted hydrochloric acid solution ($HCl:H_2O = 3:1$)

Downloaded from https://www.science.org at Konkuk University Seoul on September 19, 2024

for 1 min, an approximately 400-nm-thick covered positive-tone polymer resist (Kayaku Advanced Materials Inc., PMMA C4) was patterned in the form of an NB array comprising tethers through electron-beam lithography (EBL; Hitachi HR-SEM S-4700 modification). Following the development process, the InP sacrificial layer was etched down by applying a chemically assisted ion-beam etching process at 443 K for 30 s to the InGaAsP wafer. Last, the polymer residue was eliminated using 5-min O_2 plasma, and the remaining InP sacrificial layer under the NB arrays was removed using a diluted hydrochloric acid solution for 1 min at RT (~293 K).

The Si PhC array was fabricated on an SOI wafer, with a 280-nm-thick polycrystalline Si device layer created on top of a 3-μm SiO_2 buffered oxide layer. A positive-tone polymer resist (Kayaku Advanced Materials Inc., PMMA C4) with a thickness of approximately 400 nm was spin coated as the electron-beam resist layer. The electron-beam resist layer was patterned through EBL (Hitachi HR-SEM S-4700 modification) and subsequently dry etched using an inductively coupled plasma reactive-ion etcher (STS Multiplex ICP). Thereafter, the residual e-beam resist layer was removed using acetone and O_2 plasma.

A μ-transfer printing technique was applied to complete the fabrication of the gain-printed Si nanolaser. First, the edge of the μ-tip was aligned and supported parallel to each other. Subsequently, the XYZ translation (Newport, M-562-XYZ, DS-4F) stage was adjusted to approach the target NB. Following the establishment of a contact with the NB, the tip was pressed slightly to break the tethers, and the NB was gently separated from its growth substrate. Thereafter, the NB was registered at the Si PhC target site with high accuracy through parallelization of the μ-tip edge and Si PhC boundary. Last, the μ-tip was pressed firmly and gently moved along the axis of the NB to peel the NB from the μ-tip.

Photoluminescence analyses

The sample was firmly mounted onto a stable XYZ stage with a sensitivity of 20 nm (Newport, M-562-XYZ, DS-4F) or on a thermoelectric cooler (TEC) for cooling. To reduce the sample surface temperature by approximately 5 K, the TEC was driven using a DC power supply (UNI-T, UTP3303) of 3 V. A function generator (RIGOL, DG4162) was connected to a temperature-controlled fiber Bragg grating-stabilized laser diode with a wavelength of 976 nm (Thorlabs, BL976-P300) to generate a CW or pulse wave (1 MHz repetition rate and 100 or 500 ns pulse width). A pump beam was focused on the device using a ×50 microscope objective lens with a numerical aperture of 0.42 (Mitutoyo, M Plan Apo ×50). In addition, the light from the device was transmitted through an objective lens. Either a NIR InGaAs camera for imaging or a monochromator with a 1200 g/mm grating (Spectral Products, DK480) coupled to a femtowatt InGaAs photodetector (Thorlabs, PDF10C/M) was used for spectroscopic analysis. A tungsten halogen lamp (Thorlabs, OSL2) was used as the illumination source.

Supplementary Materials

This PDF file includes:
Supplementary Notes
Figs. S1 to S18
Tables S1 and S2

REFERENCES AND NOTES

1. A. W. Fang, H. Park, Y.-h. Kuo, R. Jones, O. Cohen, D. Liang, O. Raday, M. N. Sysak, M. J. Paniccia, J. E. Bowers, Hybrid silicon evanescent devices. *Mater. Today* **10**, 28–35 (2007).
2. G. Roelkens, J. Van Campenhout, J. Brouckaert, D. Van Thourhout, R. Baets, P. R. Romeo, P. Regreny, A. Kazmierczak, C. Seassal, X. Letartre, G. Hollinger, J. M. Fedeli, L. Di Cioccio, C. Lagahe-Blanchard, III-V/Si photonics by die-to-wafer bonding. *Mater. Today* **10**, 36–43 (2007).
3. D. Liang, J. E. Bowers, Recent progress in lasers on silicon. *Nat. Photonics* **4**, 511–517 (2010).
4. D. Thomson, A. Zilkie, J. E. Bowers, T. Komljenovic, G. T. Reed, L. Vivien, D. Marris-Morini, E. Cassan, L. Virot, J. M. Fédéli, J.-M. Hartmann, J. H. Schmid, D.-X. Xu, F. Boeuf, P. O'Brien, G. Z. Mashanovich, M. Nedeljkovic, Roadmap on silicon photonics. *J. Opt.* **18**, 073003 (2016).
5. D. Liang, J. E. Bowers, Recent progress in heterogeneous III-V-on-silicon photonic integration. *Light Adv. Manuf.* **2**, 59–83 (2021).
6. Z. Zhou, X. Ou, Y. Fang, E. Alkhazraji, R. Xu, Y. Wan, J. E. Bowers, Prospects and applications of on-chip lasers. *eLight* **3**, 1 (2023).
7. T. Mitze, M. Schnarrenberger, L. Zimmermann, J. Bruns, F. Fidorra, J. Kreißl, K. Janiak, S. Fidorra, H. Heidrich, K. Petermann, "Hybrid integration of III/V lasers on a Silicon-on-Insulator (SOI) optical board" in *IEEE International Conference on Group IV Photonics, 2005* (IEEE, 2005), pp. 210–212.
8. S. Lin, X. Zheng, J. Yao, S. S. Djordjevic, J. E. Cunningham, J.-H. Lee, I. Shubin, Y. Luo, J. Bovington, D. Y. Lee, H. D. Thacker, K. Raj, A. V. Krishnamoorthy, Efficient, tunable flip-chip-integrated III-V/Si hybrid external-cavity laser array. *Opt. Express* **24**, 21454–21462 (2016).
9. G. Roelkens, D. Van Thourhout, R. Baets, R. Nötzel, M. Smit, Laser emission and photodetection in an InP/InGaAsP layer integrated on and coupled to a silicon-on-insulator waveguide circuit. *Opt. Express* **14**, 8154–8159 (2006).
10. T. J. Karle, Y. Halioua, F. Raineri, P. Monnier, R. Braive, L. Le Gratiet, G. Beaudoin, I. Sagnes, G. Roelkens, F. Van Laere, D. Van Thourhout, R. Raj, Heterogeneous integration and precise alignment of InP-based photonic crystal lasers to complementary metal-oxide semiconductor fabricated silicon-on-insulator wire waveguides. *J. Appl. Phys.* **107**, 063103 (2010).
11. J. Van Campenhout, P. Rojo-Romeo, P. Regreny, C. Seassal, D. Van Thourhout, S. Verstuyft, L. Di Cioccio, J.-M. Fedeli, C. Lagahe, R. Baets, Electrically pumped InP-based microdisk lasers integrated with a nanophotonic silicon-on-insulator waveguide circuit. *Opt. Express* **15**, 6744–6749 (2007).
12. G. Roelkens, L. Liu, D. Liang, R. Jones, A. Fang, B. Koch, J. Bowers, III-V/silicon photonics for on-chip and intra-chip optical interconnects. *Laser Photon. Rev.* **4**, 751–779 (2010).
13. C. Xiang, W. Jin, D. Huang, M. A. Tran, J. Guo, Y. Wan, W. Xie, G. Kurczveil, A. Netherton, D. Liang, H. Rong, J. E. Bowers, High-performance silicon photonics using heterogeneous integration. *IEEE J. Sel. Top. Quantum Electron.* **28**, 10.1109/JSTQE.2021.3126124 (2022).
14. A. W. Fang, H. Park, O. Cohen, R. Jones, M. J. Paniccia, J. E. Bowers, Electrically pumped hybrid AlGaInAs-silicon evanescent laser. *Opt. Express* **14**, 9203–9210 (2006).
15. A. W. Fang, R. Jones, H. Park, O. Cohen, O. Raday, M. J. Paniccia, J. E. Bowers, Integrated AlGaInAs-silicon evanescent race track laser and photodetector. *Opt. Express* **15**, 2315–2322 (2007).
16. D. Liang, M. Fiorentino, T. Okumura, H.-H. Chang, D. T. Spencer, Y.-H. Kuo, A. W. Fang, D. Dai, R. G. Beausoleil, J. E. Bowers, Electrically-pumped compact hybrid silicon microring lasers for optical interconnects. *Opt. Express* **17**, 20355–20364 (2009).
17. D. Liang, X. Huang, G. Kurczveil, M. Fiorentino, R. G. Beausoleil, Integrated finely tunable microring laser on silicon. *Nat. Photonics* **10**, 719–722 (2016).
18. Y. Wan, C. Xiang, J. Guo, R. Koscica, M. J. Kennedy, J. Selvidge, Z. Zhang, L. Chang, W. Xie, D. Huang, A. C. Gossard, J. E. Bowers, High speed evanescent quantum-dot lasers on Si. *Laser Photonics Rev.* **15**, 2100057 (2021).
19. C. Xiang, J. Liu, J. Guo, L. Chang, R. N. Wang, W. Weng, J. Peters, W. Xie, Z. Zhang, J. Riemensberger, J. Selvidge, T. J. Kippenberg, J. E. Bowers, Laser soliton microcombs heterogeneously integrated on silicon. *Science* **373**, 99–103 (2021).
20. C. Xiang, W. Jin, O. Terra, B. Dong, H. Wang, L. Wu, J. Guo, T. J. Morin, E. Hughes, J. Peters, Q.-X. Ji, A. Feshali, M. Paniccia, K. J. Vahala, J. E. Bowers, 3D integration enables ultralow-noise isolator-free lasers in silicon photonics. *Nature* **620**, 78–85 (2023).
21. C. Xiang, J. Guo, W. Jin, L. Wu, J. Peters, W. Xie, L. Chang, B. Shen, H. Wang, Q.-F. Yang, D. Kinghorn, M. Paniccia, K. J. Vahala, P. A. Morton, J. E. Bowers, High-performance lasers for fully integrated silicon nitride photonics. *Nat. Commun.* **12**, 6650 (2021).
22. H. G. Park, S. H. Kim, S. H. Kwon, Y. G. Ju, J. K. Yang, J. H. Baek, S. B. Kim, Y. H. Lee, Electrically driven single-cell photonic crystal laser. *Science* **305**, 1444–1447 (2004).
23. K. Nozaki, S. Kita, T. Baba, Room temperature continuous wave operation and controlled spontaneous emission in ultrasmall photonic crystal nanolaser. *Opt. Express* **15**, 7506–7514 (2007).
24. H.-S. Ee, K.-Y. Jeong, M.-K. Seo, Y.-H. Lee, H.-G. Park, Ultrasmall square-lattice zero-cell photonic crystal laser. *Appl. Phys. Lett.* **93**, 011104 (2008).
25. G. Crosnier, D. Sanchez, S. Bouchoule, P. Monnier, G. Beaudoin, I. Sagnes, R. Raj, F. Raineri, Hybrid indium phosphide-on-silicon nanolaser diode. *Nat. Photonics* **11**, 297–300 (2017).
26. K. Y. Jeong, Y. S. No, Y. Hwang, K. S. Kim, M. K. Seo, H. G. Park, Y. H. Lee, Electrically driven nanobeam laser. *Nat. Commun.* **4**, 2822 (2013).

Downloaded from https://www.science.org at Konkuk University Seoul on September 19, 2024

27. R. Koscica, Y. Wan, W. He, M. J. Kennedy, J. E. Bowers, Heterogeneous integration of a III–V quantum dot laser on high thermal conductivity silicon carbide. *Opt. Lett.* **48**, 2539–2542 (2023).
28. S. Matsuo, A. Shinya, T. Kakitsuka, K. Nozaki, T. Segawa, T. Sato, Y. Kawaguchi, M. Notomi, High-speed ultracompact buried heterostructure photonic-crystal laser with 13 fJ of energy consumed per bit transmitted. *Nat. Photonics* **4**, 648–654 (2010).
29. E. Kuramochi, K. Nozaki, A. Shinya, K. Takeda, T. Sato, S. Matsuo, H. Taniyama, H. Sumikura, M. Notomi, Large-scale integration of wavelength-addressable all-optical memories on a photonic crystal chip. *Nat. Photonics* **8**, 474–481 (2014).
30. H. Jang, I. Karnadi, P. Pramudita, J.-H. Song, K. S. Kim, Y.-H. Lee, Sub-microwatt threshold nanoisland lasers. *Nat. Commun.* **6**, 8276 (2015).
31. H.-M. Kim, H. Jang, P. Pramudita, M.-K. Kim, Y.-H. Lee, Monolithic integration of self-aligned nanoisland laser with shifted-air-hole waveguide. *Opt. Express* **26**, 12569–12578 (2018).
32. J. Lee, I. Karnadi, J. T. Kim, Y. H. Lee, M. K. Kim, Printed nanolaser on silicon. *ACS Photonics* **4**, 2117–2123 (2017).
33. A. Osada, Y. Ota, R. Katsumi, K. Watanabe, S. Iwanmoto, Y. Arakawa, Transfer-printed quantum-dot nanolasers on a silicon photonic circuit. *Appl. Phys. Express* **11**, 072002 (2018).
34. M.-W. Kim, S.-W. Park, K.-T. Park, B.-J. Min, J.-H. Ku, J. S. Choi, Y.-S. No, All-graphene-contact electrically pumped on-demand transferrable nanowire source. *Nano Lett.* **22**, 1316–1323 (2022).
35. S.-W. Park, M.-W. Kim, K.-T. Park, J.-H. Ku, Y.-S. No, On-chip transferrable microdisk lasers. *ACS Photonics* **7**, 3313–3320 (2020).
36. A. L. Schawlow, C. H. Townes, Infrared and optical masers. *Phys. Rev.* **112**, 1940–1949 (1958).
37. L. A. Coldren, S. W. Corzine, M. L. Mashanovitch, *Diode Lasers and Photonic Integrated Circuits* (Wiley, 2012).
38. J. Cui, Q. Miao, P. He, B. Wang, W. Yu, Temperature dependence of refractive index change for InGaAs/InGaAsP quantum wells, in *International Photonics and Optoelectronics Meetings, OSA Technical Digest (online)* (Optica Publishing Group, 2012), paper ITh4A.24.
39. B. R. Bennett, R. A. Soref, J. A. Del Alamo, Carrier-induced change in refractive index of InP, GaAs, and InGaAsP. *IEEE J. Quantum Electron.* **26**, 113–122 (1990).
40. K. Murasawa, T. Hidaka, K. Sato, Injection-current-induced blue-shift laser diode: Concept of excess carrier conservation. *Jpn. J. Appl. Phys.* **50**, 042101 (2011).
41. Y. Wan, Q. Li, A. Y. Liu, W. W. Chow, A. C. Gossard, J. E. Bowers, E. L. Hu, K. M. Lau, Sub-wavelength InAs quantum dot micro-disk lasers epitaxially grown on exact Si (001) substrates. *Appl. Phys. Lett.* **108**, 221101 (2016).
42. Y. Wan, J. Norman, Q. Li, M. J. Kennedy, D. Liang, C. Zhang, D. Huang, Z. Zhang, A. Y. Liu, A. Torres, D. Jung, A. C. Gossard, E. L. Hu, K. M. Lau, J. E. Bowers, 1.3 μm submilliamp threshold quantum dot micro-lasers on Si. *Optica* **4**, 940–944 (2017).
43. Y. Yu, A. Sakanas, A. R. Zali, E. Semenova, K. Yvind, J. Mørk, Ultra-coherent Fano laser based on a bound state in the continuum. *Nat. Photonics* **15**, 758–764 (2021).

Acknowledgments

Funding: This work was supported by the National Research Foundation of Korea (2020R1A2C2010967 and RS-2024-00343969), Institute for Information & Communications Technology Planning & Evaluation (IITP) grant (2020-0-00947, 2022-0-00198, and 2022-RS-2022-00164799), National Research Council of Science & Technology (NST) grant (CAP22051-102), Internal grant of Electronics and Telecommunications Research Institute (ETRI) (23YS1310), KIST Institutional Program (2E32801-23-P027, and 2E32591-23-114), and KU-KIST School Project. **Author contributions:** Conceptualization: B.J.P., Y.-S.N., and M.-K.K. Fabrication silicon and III-V samples: B.J.P. and J.T.K. Transfer printing integration: B.J.P., M.-W.K., and K.-T.P. Analyzation of experimental data: B.J.P., M.-W.K., K.-T.P., B.U.Y., A.Y., Y.-S.N., and M.K.K. Developing the theoretical framework and numerical simulation: B.J.P., M.-W.K., and K.T.P. with guidance from H.-M.K., Y.-S.N., and M.-K.K.. Writing–original draft: B.J.P., M.-W.K., K.-T.P., Y.-S.N., and M.-K.K. Writing–review and editing: B.J.P., M.-W.K., Y.-S.N., and M.-K.K. **Competing interests:** The authors declare that they have no competing interests. **Data and materials availability:** All data needed to evaluate the conclusions in the paper are present in the paper and/or the Supplementary Materials.

Submitted 2 October 2023
Accepted 12 August 2024
Published 18 September 2024
10.1126/sciadv.adl1548

Downloaded from https://www.science.org at Konkuk University Seoul on September 19, 2024